Wind machines for frost damage mitigation

A quantitative 3D investigation based on observations

Dai, Yi; Boekee, Judith; Schilperoort, Bart; ten Veldhuis, Marie-Claire; van de Wiel, Bas J.H.

DOI
10.1016/j.agrformet.2023.109522

Publication date
2023

Document Version
Final published version

Published in
Agricultural and Forest Meteorology

Agricultural and Forest Meteorology 338 (2023) 109522

Contents lists available at ScienceDirect

Agricultural and Forest Meteorology

journal homepage: www.elsevier.com/locate/agrformet

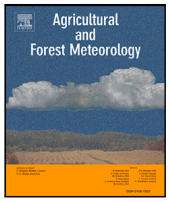

Wind machines for frost damage mitigation: A quantitative 3D investigation based on observations

Yi Dai [a,*], Judith Boekee [b], Bart Schilperoort [a], Marie-Claire ten Veldhuis [b], Bas J.H. van de Wiel [a]

[a] Faculty of Civil Engineering and Geosciences, Department of Geoscience and Remote Sensing, Delft University of Technology, Stevinweg 1, Delft, 2628CN, The Netherlands

[b] Faculty of Civil Engineering and Geosciences, Department of Water Management, Delft University of Technology, Stevinweg 1, Delft, 2628CN, The Netherlands

ARTICLE INFO

Keywords:
Frost mitigation
Wind machines
Distributed temperature sensing
Thermal inversion erosion
Turbulent flux transport

ABSTRACT

Wind machines have been increasingly used for frost damage mitigation in the agricultural community. During radiative frost nights, wind machines are used to erode near-surface thermal inversion by air mixing. The underlying mixing processes remain poorly understood. A full picture of warming effects caused by air mixing requires measurements with wide coverage and high resolution. Our study aimed to quantify the magnitude and area of warming by air mixing and identify the characteristic mixing processes downwind and upwind. We installed 9 km of fiber optic cables in a 6.75 ha orchard block, creating two horizontal planes and three vertical profiles. Quasi-3D temperature responses with spatial sampling and temporal resolution of 25 cm and 10 s, respectively, were obtained before and during machine operation. We found a 50% reduction of the local inversion strength (8 K) over 0.42 ha at 1 m and 0.46 ha at 2 m height. The warming area for a 30% reduction extends to 2.81 and 2.52 ha, respectively. As the propeller rotates 360°, the weak background wind substantially impacts the air mixing processes downwind and upwind. When jets blow along with background wind, the warming plumes arrive earlier than the jet due to horizontal advection from earlier warmed sections. The warming plumes consequently accumulate downwind and penetrate deep into the canopy. In contrast, in upwind direction, wind drag resistance causes warming plumes arrive later than the jet. Quadrant analysis reveals that flux transport during the machine operation is dominated by sweeping and ejection motions. Intermittent downdrafts of warm air and updrafts of cool air result in efficient vertical heat exchange. This feature makes wind machines highly effective in raising canopy airspace temperature to mitigate frost damage.

1. Introduction

Spring frost events have caused substantial economic losses in agricultural sectors. In 2017, spring frosts caused 3.3 billion euros of losses across Europe (Lamichhane, 2021). In France, at least half of the 680 km^2 of vineyards were damaged due to frost events in 2021 (Liubchenkova, 2021). Due to global warming, bud blooming tends to occur much earlier, while the probability of single frost nights in spring remains the same (Liu et al., 2018; Siegmund, 2022). Consequently, crop vulnerability is increasingly coinciding with the frost season. Effective methods (e.g., sprinkling, wind machines, paraffin pots) for frost mitigation remain essential to prevent crop damage.

Since the 1950s, wind machines have been increasingly used in the agricultural community to mitigate the damage of frost events (Frith, 1951; Evans, 1999). A typical anti-frost wind machine comprises a large propeller with blades of ~5-m diameter, a rotating hub, an engine to power the propeller, and a ~10-m tower to support the propeller. These anti-frost machines are theoretically designed to erode near-surface thermal inversion during radiative frost nights (Bates et al., 1978; Perry, 1998). During frost nights, the propeller thrusts large amounts of warm air downwards with a slight tilt angle to the horizontal. The warm jets create turbulent mixing along the angle of attack (Fisher, 2009; Beyá-Marshall et al., 2019). As the hub rotates, turbulent mixing erodes the inversion around the wind machine, mixing warm air aloft with colder air in the canopy. Consequently, the temperature of the affected air at canopy height rises significantly. Also, the vegetation warms as a result of the increased turbulent heat exchange (Boekee et al., 2023).

In practice, a general guideline for wind machine operations under different atmospheric conditions is yet to be developed. The difficulties are threefold. First, the magnitude and area of warming caused by machine operations are influenced by multiple factors. The warming effect is not only a function of the wind machine type (e.g., power, blades, hub height) but also depends on its operational settings (e.g., rotation period, tilting angle) and the atmospheric conditions (e.g., strength

* Corresponding author.
E-mail address: Y.Dai-1@tudelft.nl (Y. Dai).

https://doi.org/10.1016/j.agrformet.2023.109522
Received 14 October 2022; Received in revised form 3 May 2023; Accepted 16 May 2023
Available online 31 May 2023

Table 1
The warming effectiveness of horizontal-axis wind machines from previous studies. Note that N as Newton is unit of force. Please note the 50% warming in Heusinkveld et al. (2020) was the maximum relative warming, rather warming area in 3–5 ha.

Studies	Types of wind machine	Diameter of blade [m]	Hub height [m]	Tilting angle [°]	Rotation period [min]	Inversion		Effectiveness	
						Defined range [m]	Strength [K]	Position/Area	Magnitude
Brooks et al. (1952)	1068N thrust	2.74	9.75	7.5	4.5	2.1–12.2	3.3	At 2.1 m height, 36.5 m downwind	42%
	4671N thrust	6.20					3.8	From 61 m upwind to 122 m downwind	29%
Rhoades et al. (1955)	1246N thrust	2.70	12.80	7.5	4.0	3–15	3.30	No warming detected	0
	1512N thrust	3.7						0.73 ha	17%
Davis (1977)	Tropic Breeze Model S-391	5.30	10.40	7.0	4.5	1.5–18	6.40	3.4 ha; 2.1 ha; 0.8 ha	19%; 30%; 65%
Ribeiro et al. (2006)	Mecagri 19 France	5.40	10.50	7.0	4.3	1.5–15	3.00 1.70	At 1.5 m height 30 m away	67% 41%
Battany (2012)	Portable Low Crop Model; Two blades	5.00	5.90	6.0	4.5	1.1–10	1.85	At 1.1 m height 36 m away	80%
Beyá-Marshall et al. (2019)	Gas V10 model, Two solid fiberglass blades	6.00	10.67	6.0	4.5	1.5–15	3.50	At 1.5 m height 5.30 ha; 2.67ha	30%; 50%
Heusinkveld et al. (2020)	Orchard-Rite; Double blades	5.00	10.50	7.0	5.0	1–10.5	3.00	At 1 m height; 3–5 ha	50% (max)
The present study	Orchard-Rite; Double blades	6.00	10.70	8.0	5.0	1–10.7	3.00	At 2 m height; 0.46, 2.52 ha	30%, 50%

of local inversion, magnitude of wind drift) (See in Table 1). For example, Brooks et al. (1952) and Rhoades et al. (1955) found that a minimum power is required to break the inversion. The inversion strength, defined as the maximum temperature difference in the atmospheric surface layer, represents the maximum "heat reservoir" for wind machines to operate (Bates et al., 1978; Hu et al., 2018). Several studies attempted to relate the temperature response over the particular area of interest to the strength of the ambient temperature inversion near the surface (Rhoades et al., 1955; Goodall et al., 1957; Davis, 1977; Ribeiro et al., 2006). Second, in addition to the multi-factor scenarios mentioned above, warming due to air mixing under one machine type and condition exhibits a high degree of spatial–temporal variability. For example, the warming magnitude decreases with distance from the machine (Davis, 1977) and the affected area is non-symmetric due to background wind. Even with very light winds, this asymmetry can be significant as shown by Goodall et al. (1957) and Heusinkveld et al. (2020). Third, the complexities increase when a different indicator (e.g., plant temperature) is considered. The warming effects at the plant-scale depend on the heat exchange between air and plants. A detailed discussion on air-plant heat exchange during wind machine operation can be found in a companion study (Boekee et al., 2023). Our study will use air temperature as the indicator for frost protection (Perry, 1998) and focus on the first two complexities.

We tackle the aforementioned complexities in two sequential studies. The present study measures the warming effects (i.e., magnitude and area) and the spatial–temporal variability of air warming under one machine operation and atmospheric condition. A sequel study simulates various potential machine operating scenarios numerically and assesses the impact of local warming effects. The criteria of this assessment are based on the physical insights obtained in this study.

Previous studies have quantified the warming effects by a single horizontal-axis wind machine (summarized in Table 1). The magnitude of warming (hereafter effectiveness) is often defined as the reduction of thermal inversion strength (Battany, 2012; Heusinkveld et al., 2020). Most studies estimated warming magnitude and area based on several point sensors (Brooks et al., 1952, 1958), logging at coarse intervals (Brooks et al., 1954; Rhoades et al., 1955), and using interpolation (Goodall et al., 1957; Ribeiro et al., 2006; Kimura et al., 2017; Beyá-Marshall et al., 2019). Their estimations require further confirmation. The warming effectiveness depends on the interaction between the machine-ejected warming plumes and the surroundings (e.g., canopy, background wind) during 360° rotation. However, few studies have addressed the spatial–temporal variability of air mixing/warming processes or the shape of warming plumes. Using fiber optic cables, Heusinkveld et al. (2020) measured the evolution of warming plumes based on only one vertical and two horizontal profiles. They estimated the maximum warming magnitude and range based on curve fittings to a Gaussian model. While these studies provided insight into spatial–temporal variability of warming, a full picture of warming effectiveness requires measurements with wide coverage and high resolution. The underlying air mixing/warming processes remain poorly understood. Thus, the objectives of the present observational study are (1) quantifying the magnitude and area of air warming (effectiveness) by a wind machine; (2) identifying the characteristic mixing processes downwind and upwind; (3) quantifying the turbulent transport during the machine operation, an aspect not addressed in previous studies.

The measurement technique used for quantification of air mixing/warming is so-called Distributed Temperature Sensing (DTS), consisting of a network of fiber optic cables. Fiber optic cables can measure the temperature at a high spatial (sampling at 0.25 m) and temporal (10 s) resolution. We aimed to obtain quasi-3D temperature responses caused by machine operation in a 6.75 ha orchard (details in Section 2). We deployed a total length of 9 km optic cable laid out in two horizontal planes at 1 and 2 m height above the ground surface, and three vertical profiles. To analyze the measured temperature responses, we selected the operation period (on mode) and reference period (off mode) based on the general weather conditions during the experiment (Section 3.1). The warming magnitude and area caused by air mixing are demonstrated in a time-averaged view (Section 3.2). The characteristic mixing processes downwind and upwind are identified in the view of vertical and horizontal temperature evolution (Sections 3.3 and 3.4). Furthermore, the distribution of turbulent transport is quantified using Quadrant-Hole analysis at two points (Section 3.5). We obtain a three-dimensional view of temperature and flux responses caused by wind machine operation from the orchard scale to the point scale.

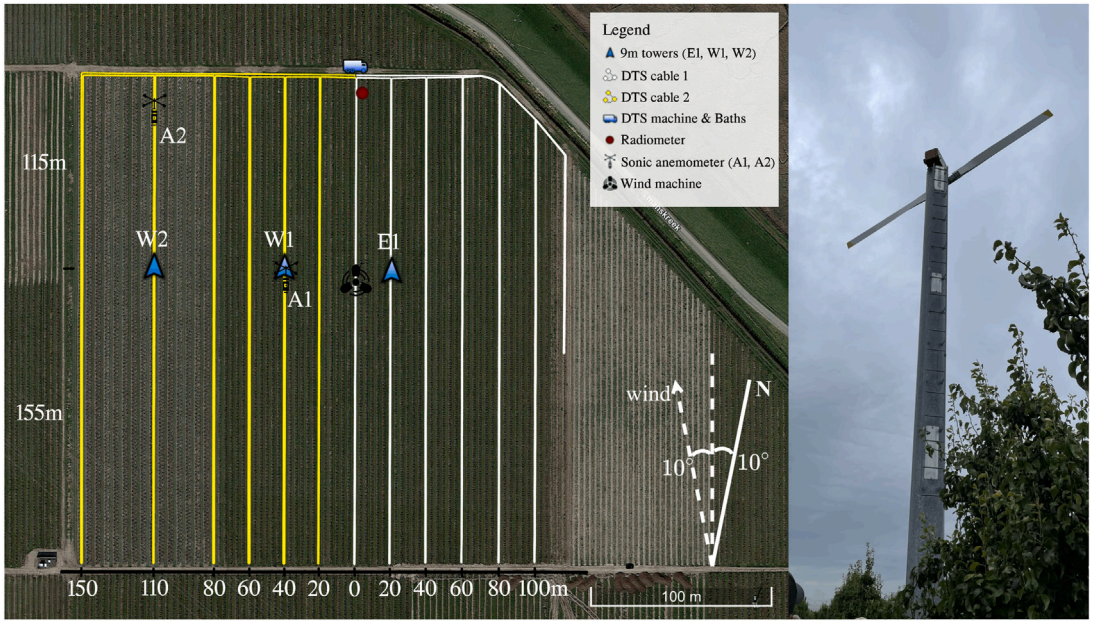

Fig. 1. The top-down view of the experimental setup (left panel). The distance of the cables relative to the wind machine and the background wind direction are indicated. The same type of cables are indicated in two colors, each approximately 4.5 km. Note that in reality each line is doubled: at 1 and 2 m height above the surface. The tree rows 80 m west to the wind machine have double trees in one row, and others have single. The wind machine in the orchard (right panel).

2. Experimental setup

2.1. Experiment site and wind machine

The field experiment was conducted on May 7–8, 2021, in a pear orchard in Krabbendijke, Zeeland, the Netherlands. Our experimental site (Fig. 1) is close to the site studied by Heusinkveld et al. (2020) yet in a different orchard block. The row orientation of the block is 10° West of North. The height of the trees and spacing of tree rows are 3 m. The tree rows 80 m west to the wind machine have double trees in one row, and others have single. In the center of the experimental block, a wind machine manufactured by Orchard-Rite was installed in November 2018. The hub height of this wind machine is 10.7 m. The rotor is composed of two straight blades and has a diameter of 6 m. A 126 kW engine Caterpillar7.1 powered the propeller. When the wind machine operates, the rotor tilts 8° downward and rotates around its vertical axis with a user-specified period of 5 min.

2.2. Instrumentation

This study used Distributed Temperature Sensing (DTS) technique to quantify the spatial and temporal variation of the temperature responses around the wind machine (Thomas et al., 2012). A typical DTS system consists of a laser controller, which shoots laser pulses through fiber-optic cables. The inhomogeneous properties of the cables result in different forms of scattering. The DTS machine can detect two distinct backscattered signals: Stokes and anti-Stokes scattering. The temperature of the cable sections can be estimated based on the intensity ratio of Stokes to anti-Stokes scattered signals after calibration to certain reference sections. The reference sections were submerged in two well-mixed cold and warm baths, and the temperature of these baths was tracked with two Pt100 temperature probes. A python package, dtscalibration v1.0.2 (des Tombe and Schilperoort, 0000), was used to calibrate the measurements (des Tombe et al., 2020). A double-end configuration was employed to better estimate uncertainty in (anti-)Stokes signals.

Fiber optical cables were connected to a Silixa Ultima-M DTS system. This system measured the cable temperatures with a reported sampling resolution of 25 cm. The integration time of measurement is set to 10 s.

In our setup depicted in Fig. 1, two fiber optic cables with a total length of 9 km and a diameter of 1.6 mm were installed along every seventh tree row to form horizontal planes at 1 and 2 m height. The horizontal spacing between the cables was 20 m, up to 30 and 40 m for the western most two rows (Fig. 1). In addition to horizontal planes, fiber optic cables were mounted to three 9 m telescopic masts. Two vertical profiles were set up on 40 m, 110 m West of the wind machine (hereafter W1, W2), and one at 20 m East (hereafter E1). Through this DTS setup, a meshed grid over 6.75 ha is obtained with a resolution of 0.25 m along the cable. The accuracy of the cable temperature is 0.1 K. This setup ensures high spatial and temporal resolution of the temperature dynamics at the orchard scale.

In our study, air temperature dynamics are *approximated* using the measured cable temperature. During nighttime, cable temperature can be lower than the air temperature due to cable longwave radiation (Schilperoort et al., 2020). We argue that our findings based on the approximated air temperature hold because relative effects are examined. We provide an estimate of the potential errors of the approximation in Appendix A. The error of relative warming magnitude (an indicator defined in Section 3.2) lies within the range of (−2.5%, +4.5%).

In addition to the temperature measurements, two ultrasonic anemometers of model YOUNG 81 000 were installed at 3 m height (Fig. 1, hereafter A1 and A2, A1 is the same position as W1). The anemometers logged the wind speed at 10 Hz with a resolution of 0.01 ms^{-1}. Based on the measurements from the anemometers, the distribution of the momentum and heat flux during the wind machine operation is quantified using Quadrant-Hole analysis (more detail in Appendix B). Furthermore, the incoming and outgoing short- and longwave radiation were measured using a CNR4 radiometer (Kipp & Zonen) installed at 2 m height (See Fig. 1).

3. Results and discussion

3.1. General weather conditions and wind machine operation

Prior to discussing the temperature responses caused by the operation, it is important to detail the weather conditions during the

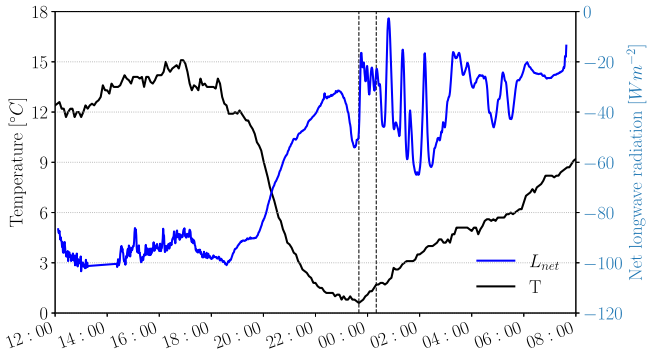

Fig. 2. Diurnal temperature cycle (black line) measured at 1.5 m height by an undisturbed weather station. Please note the observed temperature after midnight rose. The net radiative budget (blue line) on May 7–8 observed by 3 m radiometer. The selected operation period of the wind machine is indicated with the dashed lines.

experiment. A diurnal temperature cycle of about 12 °C was reported by an undisturbed weather station 1 km from the experimental orchard (not shown in the setup Fig. 1). During the day, the 1.5 m air temperature rose to 15 °C due to clear sky solar radiation. After sunset, the temperature started to cool rapidly. With near-freezing temperature, the machine started warming up at 23:00 h (with two initial cycles) and operated at full power from 23:40 h for 80 min. In the later stage of operation, some thin clouds passed over the orchard. In Fig. 2), these clouds are indicated by the large fluctuations in net longwave radiation. To avoid the influence of clouds, the first part of the operation period (23:40–00:20, dashed lines in Fig. 2)) is selected as "on" mode. During this period, minor fluctuations in the net radiation result from the periodic canopy warming by the wind machine. The period prior to operation between 22:20–23:00 is selected as undisturbed "off" mode (also shown in Fig. 6). Throughout the experiment, the background wind velocities were below 0.3 ms^{-1}, measured at 3 m height, wind direction South-East. The average relative humidity was 90%.

3.2. Air mixing effects in a time-averaged view

Fig. 3 presents the mean and spread of the temperature profiles before (off mode) and during (on mode) wind machine operation. The impact of machine operation is clearly visible in the vertical temperature profile at tower W1 (Fig. 3a) and the horizontal temperature distribution along the background wind direction (Fig. 3b). In Fig. 3a, prior to the operation, a strong inversion of 8 K near the canopy top formed due to radiative cooling of the ground surface. The uniform temperatures within the canopy (0–2.5 m) are likely a result of the net longwave radiative exchange from the canopy elements. During operation, the strong inversion was eroded by turbulent mixing, resulting in a relatively uniform vertical temperature profile. Due to periodic rotation, the spread around the mean increased in on-mode as air mixing at the sensor varied over time. The average in-canopy temperature increment induced by air mixing amounted to 3 degrees over 40 min. A similar change in the shape of the vertical profile was found by Heusinkveld et al. (2020), although the shape change at the canopy top was less pronounced. Their experiment was conducted in wintertime, within a leafless canopy. As a result, the initial inversion at the top of the canopy is much weaker than in our case, which is more typical for late spring conditions.

The horizontal distribution of temperatures at 2 m along the background wind direction shows a strong asymmetry in Fig. 3b. We attribute this to background wind advection, with a maximum velocity of 0.30 ms^{-1}. The maximum warming spot at 2 m height drifted 50 m downwind. This is explained by the momentum, heat and mass advection by background wind during the rotation. In a 5 min revolution of the turbulent jet, the background air mass at 3 m height has been replaced over a maximum distance of 90 m. Interestingly, it can be observed that even in off mode (blue) the temperature along the horizontal is nonuniform over the field. For instance, a relatively higher temperature around the orchard edges and a sudden peak at 70 m downwind are observed. This can be caused by heterogeneous heat exchange process due to either local field properties or by non-uniform surroundings. Near the orchard edges, more frequent heat exchange occurs due to exposure to the wind. Similarly, the double-tree rows arrangement at 70 m downwind exert high wind shear just above the canopy. This results in more frequent sweeping motions within canopy airspace and efficient heat exchange. However, it is difficult to substantiate this effect with our data.

As different studies on air mixing by wind machines are subjected to different background inversions, usually the *normalized warming* (NW) $\Delta T/\Delta T_{\max}$ in Eq. (1) is considered to quantify the temperature responses. It is the ratio between the actual temperature increment induced by the wind machine (ΔT) and the maximum increment ($\Delta T_{\max}$) that can be ideally achieved (Beyá-Marshall et al., 2019; Heusinkveld et al., 2020).

$$\frac{\Delta T}{\Delta T_{\max}} = \frac{[T_{on}(\vec{r},h,t) - T_{off}(\vec{r},h,t)] - [T_{on,ref}(h,t) - T_{off,ref}(h,t)]}{T_{hub} - T_{off}(\vec{r},h,t)} \quad (1)$$

where h is the height and $\vec{r}$ is horizontal location vector. The normalizer $\Delta T_{\max}$ is compared to the temperature at hub height, T_{hub}. In Fig. 3a, $\Delta T_{\max}$ is the difference between the black dashed line T_{hub} and the blue dotted line T_{off}. ΔT is the difference between the red and blue dotted lines. However, the temperature difference between these two modes might result from the warming by air mixing and (or) the nighttime cooling. To compute the actual temperature responses by the wind machine, the overall nighttime cooling trend needs to be accounted for. The cooling effects over the field are corrected by subtracting the temperature difference in the reference section $[T_{on,ref}(h,t) - T_{off,ref}(h,t)]$. In our case, the reference section is chosen as the undisturbed cable section at the southeast corner.

Fig. 4 shows horizontal contours of the *normalized warming* during operation. The contours are averaged over a 40 min operation period. To the best of our knowledge, the present study is the first to measure a full picture of warming effectiveness with a high resolution over such a large area. Normalized warming ≥50% is achieved over an area of 0.42 and 0.46 ha at 2 and 1 m height, respectively. For 30% normalized warming, the area extends to 2.81 and 2.52 ha, respectively. The coverage area is smaller than reported in the literature (See Table 1) due to the exceptionally large inversion strength (8 K) in our measurement night. The non-symmetrical shape of the averaged warming plume is explained by the background wind drifting, resulting in a larger warming area downwind. The drifting effect is more pronounced at 2 m, closer to the top of the canopy.

The relationship between the *normalized warming* and the corresponding warming area is summarized in Fig. 5. As expected, the cumulative warming area monotonically decreases with increasing warming magnitude. Note that the definition of Eq. (1) (illustrated in Fig. 3) prevents a normalized warming of 100% even in case of perfect mixing. This is due to the fact that the canopy temperature can never reach the hub height temperature as the cold air below is thermodynamically distributed over the lowest 10 m. Hence, the after-mixing temperature will always be lower than the initial hub height temperature. The warming area at two heights was similar for higher warming magnitudes (≥35%). For relative lower warming, a larger area is affected at 2 m. This is expected because the plume has to penetrate from above. Since our DTS network does not fully cover the warming plume (see 30% contour line in Fig. 4), the areas of normalized warming below 30% are slightly underestimated.

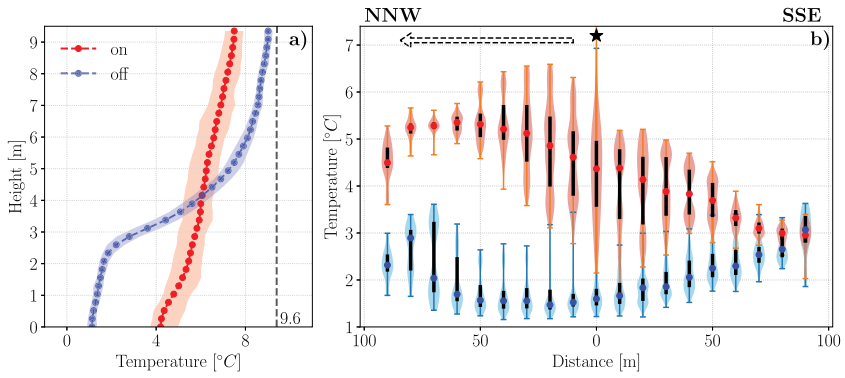

Fig. 3. (a) The mean and spread of vertical temperature profile during the 40 min of on (red) and off (blue) mode at tower W1. The dashed line indicates the extrapolated temperature 9.6 °C at hub height 10.7 m. (b) The on (red) and off (blue) mode horizontal temperature distribution at 2 m height along the direction of the background wind, which is indicated by a dashed arrow (SSE to NNW). The distance is relative to wind machine location (black star). The median temperature is marked with dots. The 25% and 75% percentiles are indicated with black sold lines.

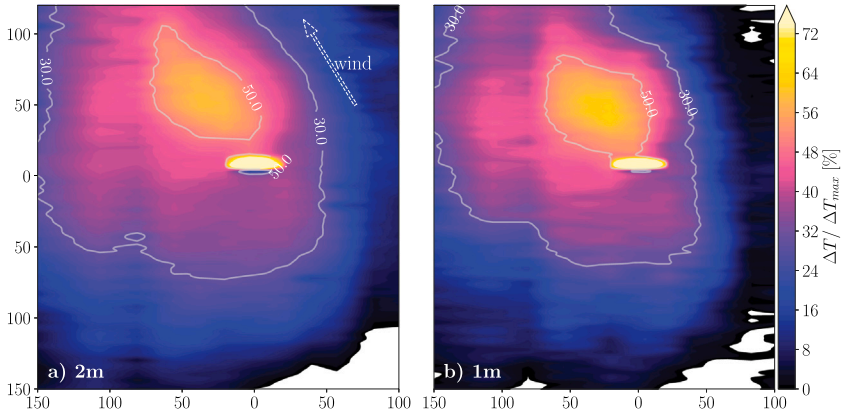

Fig. 4. Planar view of the time-averaged normalized warming in the upper and lower canopy at 2 and 1 m height. The *normalized warming* contours of 50% and 30% are indicated with white contour lines. The wind machine was located in the middle of the field, where the high temperature spot was. This is caused by the heat and radiation emission of the machine engine. The background wind direction is indicated with the white dashed arrow (maximum 0.30 m/s at 3 m).

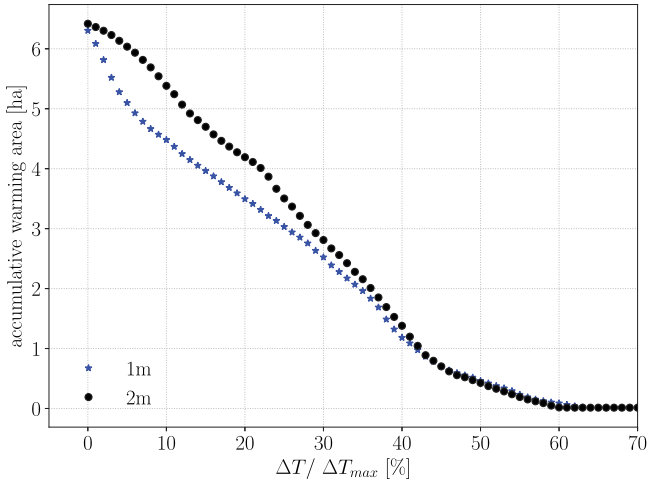

Fig. 5. The relationship between time-averaged *normalized warming* and accumulative warming area at two heights. Notice that the results for the different heights are comparable, with the warmed area a little larger at 2 m.

3.3. Air mixing processes: vertical temperature evolution

The temperature time series at 1 and 9 m height of tower W1 are shown in Fig. 6a and the corresponding temporal variation of the profile is shown in Fig. 6b. During off mode, a strong thermal inversion is established, with sharp gradient at the canopy top (see also Fig. 3). The formation of the cold canopy layer prior to motor operation likely results from longwave cooling redistribution by the tree elements and blocked turbulent exchange with the 'open air' due to tree confinement. Next, as the temperature approached the freezing point, the machines started to operate in an intermittent (warm-up) mode. The warming effect of the first two rotations is remarkably strong, with instantaneous warming of 4 and 6 °C during the first and second cycle. The relatively warmer plumes originate from the undisturbed warmer air at the upper height. After the start-up mode, the wind machine entered the full operation mode and started rotating. Now the air is mixed each time the jet passes by. As a result, the temperature becomes more uniform (Fig. 6a): the air temperature within the canopy increases at the expense of the air above the canopy. Furthermore, Fig. 6a (blue line) shows that the rotation time is short enough to keep the in-canopy temperatures above 5 °C for the remaining period.

Phase-averaged temperature profiles at three towers are shown in Fig. 7. These profiles are aligned relative to the time of wind machine jet passage, when the maximum wind velocity occurs. When the jets blow against the background wind at tower E1, the warming plumes arrive after jet passage. This delay time is probably caused by the wind drag. In contrast, the downwind masts (W1, W2) experience warming before the jet (core) arrives. We attributed this early warming to the advection of earlier warmed sections. As a result of advection, the warming magnitude is larger at tower W1 than at E1, even though tower E1 is closer to the wind machine. This difference indicates the plumes penetrate deeper and get better mixed along the background wind direction. In contrast to the downwind area, the warming plumes

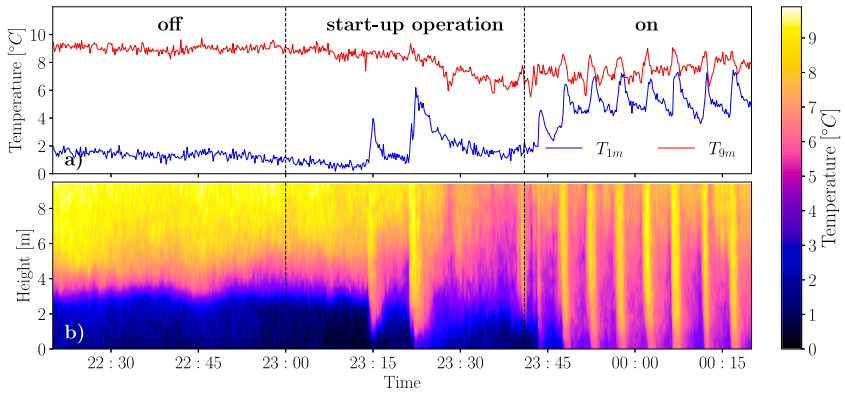

Fig. 6. (a) The time series of the 9 m and 1 m temperature at tower W1. (b) The contour plot of temporal temperature variation at tower W1. Three phases of the wind machine operation are indicated: off, start-up operation (intermittent), and fully on period.

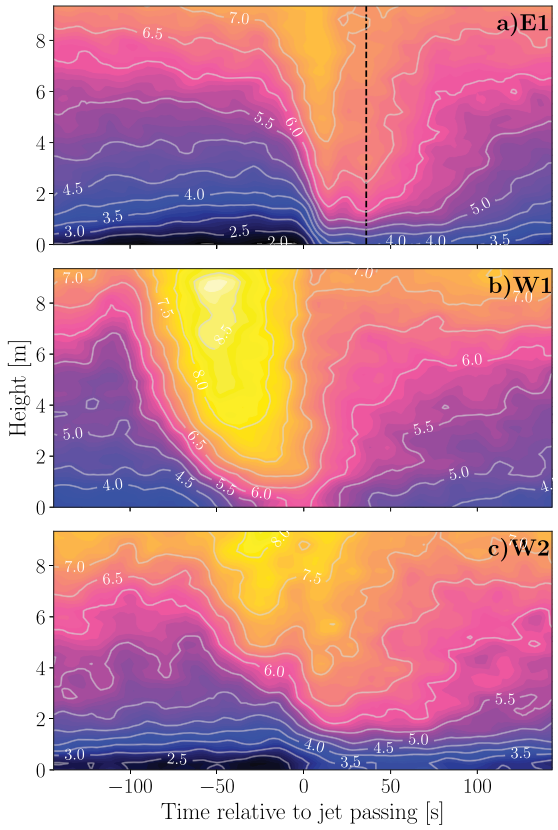

Fig. 7. As a function of time: the phase-averaged temperature profile at tower (a) E1, (b) W1, and (c) W2. The temperature magnitude is indicated by the contour lines and the labels. The dashed black line in (a) indicates the formation of a secondary warming plume.

upwind (tower E1) were *uplifted* by the weak background wind (flow convergence). Furthermore, a second warming plume seems to develop right after the central plume at E1 (black dashed line in Fig. 7a). This secondary warming plume indicates the formation of turbulent vortices, which act to recirculate the uplifted warming plumes down. Those effects were found in numerical simulations of the present case, which will be presented in follow-up work.

The spatial–temporal autocorrelation function is used to detect the thermal periodicity and coherence induced by the wind machine. By definition, the self-correlation function characterizes the spatial and temporal similarity of the observations with its delayed copy. The normalized correlation function for a variable φ is defined as

$$R(\Delta x, \Delta t) = \frac{\overline{\varphi'(x,t)\varphi'(x+\Delta x, t+\Delta t)}}{\sqrt{\overline{\varphi'(x,t)^2}} \cdot \sqrt{\overline{\varphi'(x+\Delta x, t+\Delta t)^2}}} \tag{2}$$

where $\varphi'(x,t)$ is the fluctuation with respect to the mean of quantity $\varphi(x,t)$. The autocorrelation of the temperature time series gives information about the structure of thermal plumes. Furthermore, the integral time scale T_{int} in Eq. (3) can be estimated by integrating the correlation coefficient at a fixed location $R(\Delta x = 0, \Delta t)$ with respect to the time lag Δt direction.

$$T_{\text{int}} = \int_0^{\infty} R(\Delta x = 0, \Delta t) d\Delta t \tag{3}$$

As to avoid the periodic influence of the wind machine, T_{int} here is approximated with the integral up to the first zero-crossing point. T_{int} indicates the characteristic decorrelation time at one measurement point (Oliver, 2012). Specifically in this study, it is the characteristic traveling time of the dominant features through the measurement points.

In this study, temperature time series at each height during the operation (on-period in Fig. 6) are taken as input for the autocorrelation function (Eq. (2)). Fig. 8 shows the contours of the correlation coefficient at three towers. Larger absolute correlation coefficients indicate stronger periodicity. Hence, the color's shade represents the strength of the autocorrelation, indicating the rotating plumes' periodic effects. As depicted in Fig. 8bc, the clear periodicity in the downwind western masts directly results from the wind machine operation. In contrast, the periodicity on eastern mast is absent at higher heights (Fig. 8a). This disparity might be attributable to the plumes blowing against the background wind. We speculate that the ambient wind uplifts and recirculates these warm plumes. As also shown earlier (Fig. 7a), the formation of the second warming plume was found in the phase-averaged temperature signals. The autocorrelation function did not clearly detect these circulated plumes near E1, likely due to its irregular pattern and relative low-temperature magnitude at higher heights. Signs of similar vortex-wave structures were detected further downwind. These signs are apparent in Fig. 8bc but obscured in Fig. 7bc. At the higher height of W1, for example, the warming waves recurred at half of the rotation cycle. At 110 m downwind (Tower W2), the signals of the warming plumes and recirculated vortex were both weakened because of diffusion over distance.

The integral time scale is calculated from Eq. (3), by integrating $R(\Delta x = 0, \Delta t)$ up to the first zero-crossing point (See Fig. 8). Fig. 9 shows the profiles of the integral time scale at three towers. The integral time scale indicates the observed passing time of the rotating warming plume at the measurement points. Here this characteristic passing time just above the canopy seems to be around 36 s. The integral time scale

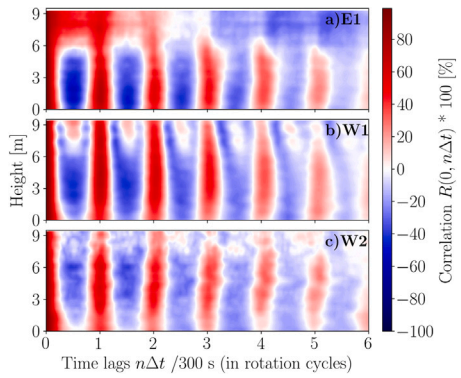

Fig. 8. The contours of the correlation coefficient for all height along the towers.

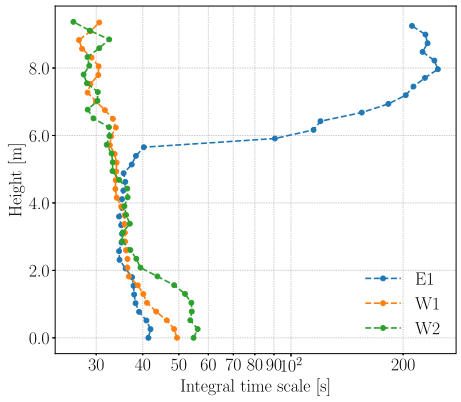

Fig. 9. The profiles of the integral time scale T_{int} at three towers.

had similar profiles downwind (W1, W2) except for the region within the canopy (lower 3 m). The traveling speed of thermal plumes slowed down from top to bottom due to vertical momentum diffusion (canopy drag). The thermal plumes at W1 traveled faster than at W2 because warm plumes diffused/broadened over distance. For the tower upwind (E1), a similar behavior is observed below 6 m. However, higher up at E1, the integral time scale was particularly large due to non-periodic mixing.

3.4. Air mixing processes: horizontal temperature distribution

Where an overall time-averaged perspective of warming plumes is presented in Fig. 4, instantaneous movies of the warming plume show an interesting spiral type of behavior (shown in supplementary material Appendix C). Here, snapshots of warming plumes are *phase-averaged* to emphasize statistical significance. Four representative moments (jets downwind, upwind, left, and right cross-wind) of the phase-averaged *normalized warming* are displayed in Fig. 10. The shape of the warming plumes was initially hypothesized to be a spiral (Brooks et al., 1952) and later on an expanding toroidal ring (Brooks et al., 1958). When the jet blows along the background wind, the shape of the warming plume likely matches the shape of a spiral. In other cases, we observed that the plume shape was distorted by the background wind and the warming air was drifted downwind. As a result, warming plume tends to accumulate downwind, resulting in a larger warming area. Furthermore, there is a time delay between the wind jet and the warming plume due to background wind. This delay feature was also shown in Fig. 7.

To show the mixing processes along the horizontal profiles, Fig. 11 documents the temporal variation of the normalized warming along and across the background wind direction, respectively. On top of the temporal variation plots, the integral time scale is plotted as a function of distance. Based on Fig. 11a, the influenced distance ranged from 80 m upwind to more than 130 m downwind. The relatively larger time scale downwind is the result of slow and irregular plume accumulation due to horizontal advection. Along the cross-wind direction, the warming plumes cover the range of 120 m left to 60 m right. We attribute this cross-wind asymmetry to the rotation direction of the wind machine. When the plume reaches the leftmost side, the plume prior to this time-step undergoes an acceleration process. This results in a longer reaching distance to the left. Conversely, the plume is decelerating before the plume reaches the far right and therefore has a relatively short reaching distance.

3.5. Air mixing processes: turbulent transport distribution

To characterize local air mixing processes, so-called Quadrant-Hole (hereafter QH) analysis is performed on the turbulent flux. Specifically, we use QH analysis to compare the relative distribution of vertical momentum and heat fluxes before and after the wind machine operation at two anemometer locations (Fig. 1, A1 and A2). The technique of QH analysis has been used in canopy studies to investigate the turbulent transport of momentum, heat, and moisture (see a list of applications in Brunet (2020, Chapter 3.1)). Since the method of QH analysis is well described in the literature (Lu and Willmarth, 1973; Yue et al., 2007), we succinctly illustrate it here with an example. More details can be found in Appendix B.

In Fig. B.13, the events of x-component momentum flux defined by QH are "outward interaction" (Q1), "ejections" (Q2), "inwards interaction" (Q3), and "sweeps" (Q4), respectively. For instance, the sweep events are characterized by fast air parcels ($u' > 0$) transporting downwards ($w' < 0$). The events of heat flux in Q1, Q2, Q3, and Q4 are defined as "warm updraft", "cool updraft", "cool downdraft", and "warm downdraft", respectively. The flux values in each quadrant are sampled with H-th percentile of its distribution. As the hole size H increases, the flux events are more extreme and its frequency decreases. The intensity and frequency of flux events are quantified using the *value fraction* $S_{i,H}$ and *duration fraction* $t_{i,H}$, respectively (Appendix B).

The *values fraction* $S_{i,H}$ is computed in the on and off mode. Fig. 12 presents the *values fraction* of sensible heat flux (upper panel) and x-component momentum flux (lower panel) at the positions A1 (left panel) and A2 (right panel) (Fig. 1). For sensible heat flux (upper panel) during the operation, a larger proportion of warm downdraft motions (Q4) contributed to the total heat transport at both A1 and A2. This is due to the fact that the jet is inclined slightly downward and also likely due to (KH-type of) flow instabilities induced by the jet. For cool updraft motions (Q2), the relative ratio increased in A2 and decreased in A1. As A1 is closer to the machine, one speculation is that the air plumes perceived at A1 diffused less and still kept the direction of the rotor (i.e., 8° downward tilting). Then, there is relatively less contribution of cold updraft motion at A1.

The motions of warm downdraft and cool updraft can be beneficial for the erosion of thermal inversion. The parameter $(S_{2,0} + S_{4,0}) / (S_{1,0} + S_{3,0})$ in Table 2 indicates the ratio between stratification eroding (Q2 and Q4) and stratification restoring (Q1 and Q3) motions. It is not surprising that $(S_{2,0} + S_{4,0}) / (S_{1,0} + S_{3,0})$ was more significant during the on mode. Furthermore, the warm downdraft motions ($S_{4,0}$) contributed more than the motions of cool updraft ($S_{2,0}$) during the on mode at both positions. This higher proportion becomes more pronounced when only the most intensive events are considered ($S_{4,H'}/S_{2,H'}$), where H' is the hole size where half of the flux occurs. The heat flux with a magnitude larger than hole size $H' > 3$ accounted for only 7% of the time ($\sum_{i=1}^{4} t_{i,H'}$). The distribution indicates that the heat transport processes caused by wind machine operation are efficient and intermittent. Similar conclusions were drawn in canopy studies (Raupach, 1981; Raupach et al., 1986).

Since the findings of momentum flux are quite similar to heat flux, we will discuss it succinctly. During wind machine operation,

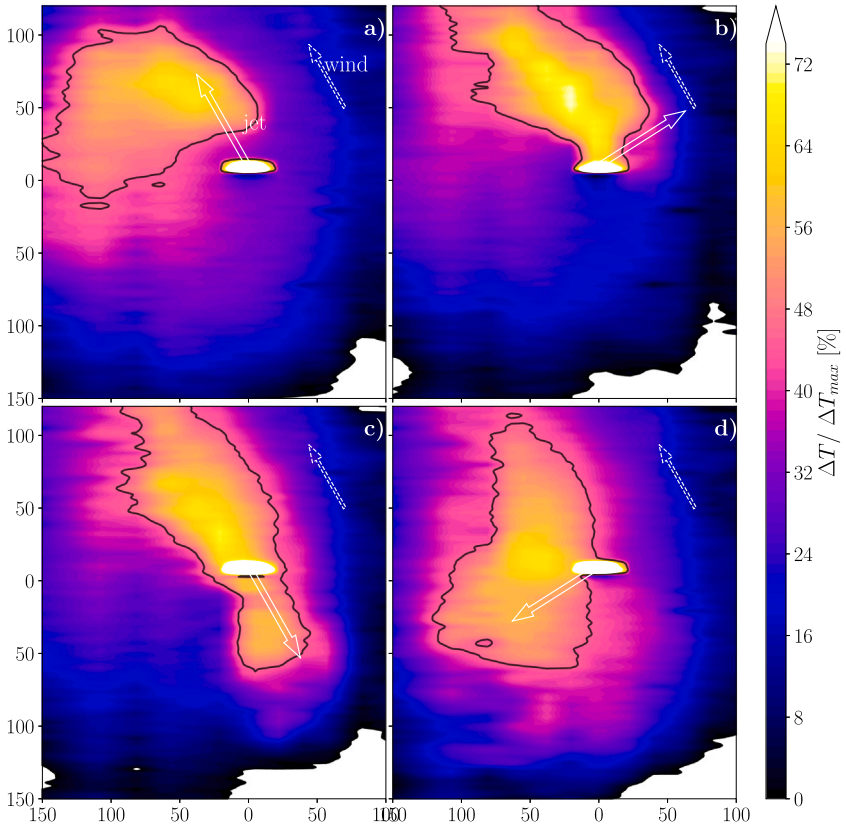

Fig. 10. Four moments of the phase-averaged *normalized warming* at 2 m height: jet (large white arrow) (a) downwind, (c) upwind, (b) right and (d) left of the cross-wind relative to the background wind direction (small dashed arrow). The black contour line indicates a 45% reduction of the ambient inversion.

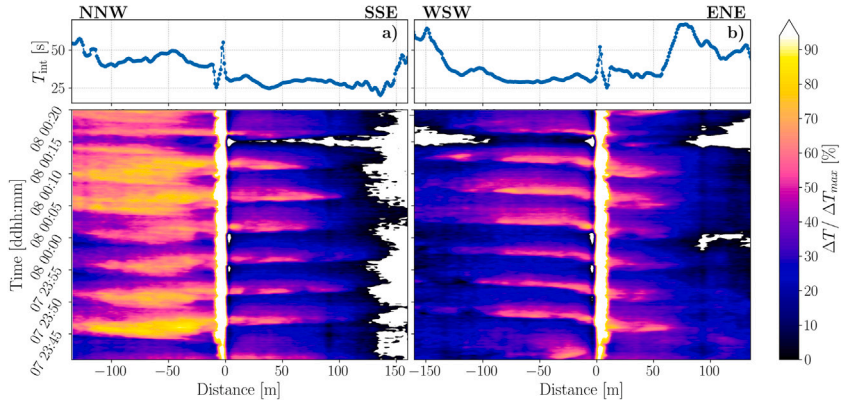

Fig. 11. Left panel: (a) Along the wind direction: normalized warming. Right panel (b) Across the wind direction: normalized warming. In the upper panel the integral time scale as a function of distance is displayed (Eq. (3)).

Table 2
Parameters related to the Quadrant-Hole analysis for sensible heat flux at sonic anemometers A1 and A2.

Cases	A1 - on	A1 - off	A2 - on	A2 - off
$(S_{2,0} + S_{4,0}) / (S_{1,0} + S_{3,0})$	1.81	1.62	3.99	0.82
$S_{4,0}/S_{2,0}$	1.25	1.02	1.41	1.04
H'	3.1	3.1	3.0	2.0
$\sum_{i=1}^{4} t_{i,H'}$	0.069	0.078	0.078	0.136
$S_{4,H'}/S_{2,H'}$	2.23	1.21	1.99	0.67

Table 3
Parameters related to the Quadrant-Hole analysis for momentum flux (x-component) at sonic anemometers A1 and A2. Note that there where no ejections larger than half the hole size for S1 during on mode, which results in an infinite $S_{4,H'}/S_{2,H'}$.

Cases	A1 - on	A1 - off	A2 - on	A2 - off
$(S_{2,0} + S_{4,0}) / (S_{1,0} + S_{3,0})$	6.28	1.41	3.69	0.94
$S_{4,0}/S_{2,0}$	4.44	1.05	1.68	1.01
H'	19.9	2.7	3.6	2.0
$\sum_{i=1}^{4} t_{i,H'}$	0.011	0.094	0.061	0.145
$S_{4,H'}/S_{2,H'}$	inf	1.27	3.30	0.72

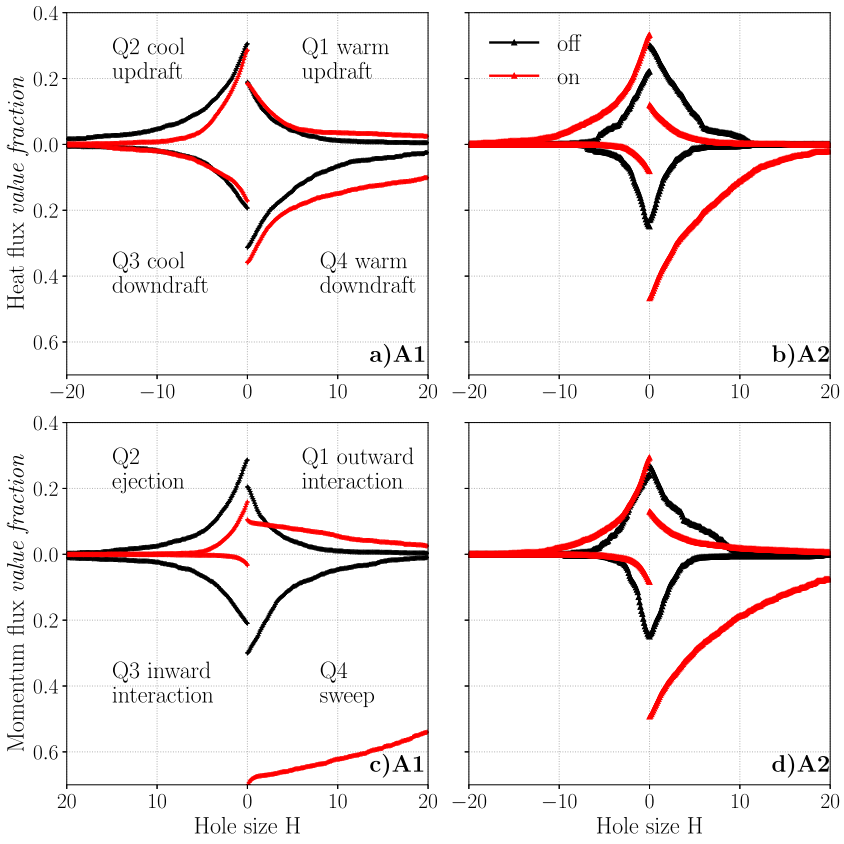

Fig. 12. The quadrant analysis of *value fraction* of the heat flux (upper panel) and momentum flux (lower panel) at positions of sonic anemometers A1 (left panel) and A2 (right panel). The red and black lines represent the on and off mode respectively.

the motions of sweeping and ejection ($(S_{2,0}+S_{4,0})/(S_{1,0}+S_{3,0})$ in Table 3) dominated the momentum transport. There appears to be a strong similarity between the behavior of downward heat and momentum fluxes. Due to the machine operation, the air mixing processes mainly developed with fast air parcels sweeping downward and slow air parcels ejecting upward. Correspondingly, in the presence of inversion, there are downdrafts of warm air and updrafts of cool air. In summary: the Quadrant-Hole analysis shows that there is a dominant role of wind-machine-induced downward sweeps in transporting both heat and momentum.

4. Conclusion

The present study aims to quantify the warming effects (i.e., magnitude and area) of wind-machine induced air mixing, identify the characteristic mixing processes downwind and upwind, and quantify the turbulent flux during the wind machine operation. Using a total length of 9 km fiber optic cable, we measured quasi-3D temperature responses at 25 cm sampling and 10 s temporal resolution over a 6.75 ha orchard. We summarized the characteristics of air mixing in a time-averaged and an instantaneous view. The flux distribution caused by wind machine is quantified using Quadrant-Hole analysis. We conclude:

- The warming effects caused by wind-machine induced air mixing shows a high degree of spatial–temporal variability. We found a 50% reduction of the local inversion strength (8 °C) over 0.42 ha at 1 m and 0.46 ha at 2 m height. For a 30% reduction, the coverage area spread to 2.81 and 2.52 ha, respectively. On average, wind machine operation raised in-canopy temperature by 3 K, during a period of 40 min.
- As the propeller rotates 360°, the weak background wind substantially impacts the air mixing processes downwind and upwind. When jets blow along with background wind, the warming plumes arrive earlier than the jet due to horizontal advection from earlier warmed sections. The warming plumes consequently accumulate downwind and penetrate deep into the canopy. In contrast, in upwind processes, wind drag resistance is felt and warming plumes arrive later than the jet. We speculate that these warming plumes are uplifted due to flow convergence and then recirculated by the ambient wind.
- Quadrant analysis reveals that flux transport during operation is dominated by sweeping and ejection motions. Intermittent downdrafts of warm air and updrafts of cool air result in efficient vertical heat exchange. This feature makes wind machines highly effective in increasing canopy airspace temperature to mitigate frost damage.

In this study, we only investigated the spatial–temporal variability of air warming under one machine type and one specific, given weather condition (possible thin-cloud condition). While the observed features like “inversion erosion” and “plume drifting” agree with the literature, we hope to provide more experimental evidence for various night conditions in future studies. In addition, more wind field measurements coupled with temperature data will help to understand the heat exchange between air and plant tissue (Boekee et al., 2023).

In a companion study, we simulate various potential operation scenarios (e.g., tilting angle, rotation period) numerically and assess the impact of local warming effects. Along with the present observational study, an enhanced physical understanding of the turbulent mixing processes in a complex environment may help to assess both the potential and the limitations of this emerging frost mitigation method.

Declaration of competing interest

The authors declare that they have no known competing financial interests or personal relationships that could have appeared to influence the work reported in this paper.

Data availability

The measurement data are open in 4TU.ResearchData repository (DOI: 10.4121/20583801).

Acknowledgments

The authors are grateful to Martijn Vogelaar for the experimental site. We would also like to thank Myrthe Breedijk, Antoon van Hooft, Koen Harms, Rik Aulbers, Rene Reudink, and Shihao Wang for their efforts in the experimental setup. We thank Steven van der Linden for constructive comments on the manuscript, Ned Patton and John Finnigan for general discussion on canopy flows. Yi Dai likes to thank Sukanta Basu for the suggestion on the integral time scale. Finally, we thank the Dutch Research Council NWO for the project funding (EN-WSS.2018.006)

Appendix A. Error analysis

The measured temperature by DTS cables without shielding or active ventilation often can be slightly lower than air temperature during nighttime (Schilperoort et al., 2020). Due to longwave radiative cooling or heat exchange, systematic errors will occur. Together with the uncertainty of temperature measurement itself, the total error will propagate in derived parameters such as the *normalized warming*.

This section estimates the total error of *normalized warming* $\Delta T/\Delta T_{\max}$ (NW in Eq. (1)) using error propagation. The total error of *normalized warming* is composite of the uncertainty σ_{NW} and systematic offset S_{NW} of *normalized warming*. Based on Eq. (1), the uncertainty σ_{NW} can be expressed in Eq. (A.1), where the cross-terms are neglected.

$$\frac{\sigma_{NW}}{\Delta T/\Delta T_{\max}} \approx \sqrt{[\left(\frac{\sigma_{\Delta T}}{\Delta T}\right)^2 + \left(\frac{\sigma_{\Delta T_{max}}}{\Delta T_{max}}\right)^2]}, \tag{A.1}$$

where $\sigma_{\Delta T}$ and $\sigma_{\Delta T_{max}}$ are the variances of ΔT and ΔT_{max}, respectively. There are given by

$$\sigma_{\Delta T} = \sqrt{\sigma^2_{T_{on}} + \sigma^2_{T_{off}} + \sigma^2_{T_{on,ref}} + \sigma^2_{T_{off,ref}}} \tag{A.2}$$

$$\sigma_{\Delta T_{max}} = \sqrt{\sigma^2_{T_{hub}} + \sigma^2_{T_{off}}} \tag{A.3}$$

For every cable measurement, the uncertainty is the accuracy of measured temperature σ_T, which is 0.1 K. Then, $\sigma_{\Delta T}$ equals to 0.20 K and $\sigma_{\Delta T_{max}}$ equals to 0.14 K in Eqs. (A.2), (A.3). Based on Eq. (A.1), the averaged σ_{NW} calculated for 2 m and 1 m are ±2.3% and ±1.9% respectively.

For systematic offset S_{NW}:

$$\frac{S_{NW}}{\Delta T/\Delta T_{\max}} \approx \frac{S_{\Delta T}}{\Delta T} - \frac{S_{\Delta T_{\max}}}{\Delta T_{\max}} \tag{A.4}$$

With:

$$S_{\Delta T} = (S_{T_{on}} - S_{T_{off}}) - (S_{T_{on,ref}} - S_{T_{off,ref}}) \tag{A.5}$$

$$S_{\Delta T_{max}} = S_{T_{hub}} - S_{T_{off}} \tag{A.6}$$

where S_T is the corresponding systematic offset for cable temperature at different periods and sections. Schilperoort et al. (2020) estimated the offset by comparing the temperature of unshielded cables to measurements from a psychrometer. The offset varies under different conditions of longwave radiation and wind speed. Specifically, the offset during the on mode $S_{T_{on}}$ can be different in ($S_{T_{on,in}}$) or outside ($S_{T_{on,out}}$) the influenced area. In our study, the averaged net longwave radiation during the off and on mode are −33 W m^{-2} and −27 W m^{-2} respectively (see Fig. 2). The average wind speed is around 0.30 m s^{-1} during off mode. During on mode, the average wind speed in the influenced area is approximated as 3 m s^{-1}. Following Schilperoort et al. (2020), $S_{T_{on,in}}$ is estimated to be −0.05 K, and $S_{T_{on,out}}$, $S_{T_{on,ref}}$ are approximated to be −0.20 K, where the minus sign indicates lower temperature relative to air temperature. During the off mode, $S_{T_{off}}$, $S_{T_{off,ref}}$, $S_{T_{hub}}$ are approximated as −0.30 K. Based on Eqs. (A.4)–(A.6), the averaged systematic offset for the *normalized warming* in ($S_{NW,in}$) or outside ($S_{NW,out}$) the area of influence are +2.2% and 0% respectively. Please note that $S_{\Delta T_{max}}$ always approaches to zero due to same offset of $S_{T_{hub}}$ and $S_{T_{off}}$.

In summary, the error of the *normalized warming* is expected to lie within the range of (−2.5%, +4.5%) at 2 m and (−1.6%, +3.8%) at 1 m based on error propagation calculation.

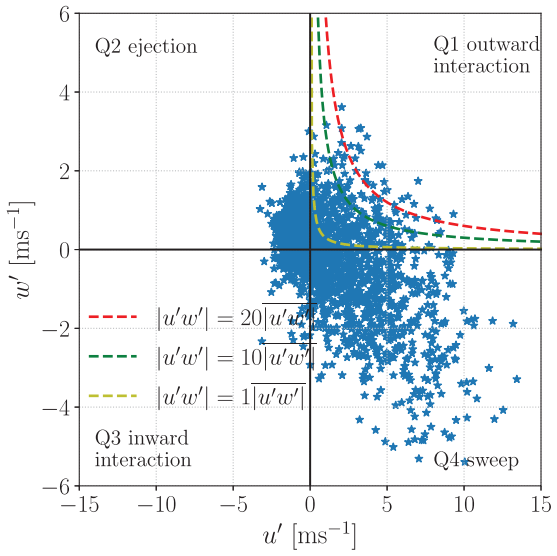

Fig. B.13. A schematic of quadrant events based on the x-component of momentum flux measured at A1 during on mode and three examples of hole region (H = 20, 10, 1). Points outside the hole regions indicate the flux contribution for each hole sampling.

Appendix B. Description of Quadrant-Hole (QH) analysis

The QH analysis divides the fluxes into four quadrants (hereafter Q1, Q2, Q3, and Q4) based on the signs of two individual flux-component quantities (such as w and u in the momentum flux). For the x-component of momentum flux displayed in Fig. B.13, for example, the flux contributions can be decomposed as (Lu and Willmarth, 1973; Yue et al., 2007):

Q1 when $u' > 0, w' > 0$, outward interaction
Q2 when $u' < 0, w' > 0$, ejections
Q3 when $u' < 0, w' < 0$, inwards interaction
Q4 when $u' > 0, w' < 0$, sweeps

For instance, the events of slow air parcel ($u' < 0$) moving upwards ($w' > 0$) are ejections. The sweeps events are characterized by fast air parcel ($u' > 0$) transporting downwards ($w' < 0$). In contrast, the motions of heat flux are sometimes defined differently in literature. To avoid confusion, we here adapted the definition from Lee and Black (1993). The events of heat flux in Q1, Q2, Q3, and Q4 are defined as “warm updraft”, “cool updraft”, “cool downdraft”, and “warm downdraft”, respectively.

To further characterize flux distributions in each quadrant, Hole Analysis, a conditional sampling technique, partitions the fluxes outside the holes based on the magnitude of fluxes. Here the partition condition is based on the time-averaged absolute value of fluxes $|\overline{u'w'}|$ and the hole size H. For example, outside the hole implies:

$$|u'w'| \geq H|\overline{u'w'}| \tag{B.1}$$

Next, the averaged flux $\overline{|u'w'|}$ is chosen as the normalizer and the value is fixed in each scenario. Then, the flux distribution is a function of the hole size, and in this way the contribution of extremes to the flux is characterized. As the hole size H increases, the events of the fluxes have less chance of falling outside of the hole, and the significance of the instantaneous flux to the mean is relatively higher (Fig. B.13). To group the flux events in each quadrant and hole size, a conditional function $I_{i,H}(u'w')$ is introduced

$$I_{i,H}\left(u',w'\right)=\begin{cases}1, & \text{if } \left(u'w'\right) \text{ is in quadrant } i \text{ and } \left|u'w'\right|\geq H\left|\overline{u'w'}\right| \\ 0, & \text{otherwise}\end{cases} \tag{B.2}$$

In Fig. B.13, for example, $I_{1,10}$ equals one when the fluxes events fall in Q1 and outside the green dashed line. The values of the grouped fluxes in each quadrant (i th), as a function of hole size H, are summed and then normalized by the total fluxes:

$$S_{i,H}=\frac{\int_0^{T_{sp}}|u'w'(t)|I_{i,H}\left(u',w'\right)dt}{\int_0^{T_{sp}}|u'w'(t)|dt} \tag{B.3}$$

where the normalized fluxes, called the fluxes *value fraction* $S_{i,H}$, in Eq. (B.3) is similar to the definition in Yue et al. (2007) in a different format. T_{sp} is the sampling period. Since the absolute values of the fluxes during the on mode are much larger than the off mode due to machine operation, here only relative distributions of the motions in each operation mode are compared. Furthermore, the frequency of the fluxes events in each quadrant or hole is assessed by the *duration fraction* $t_{i,H}$.

$$t_{i,H}=\frac{1}{T_{sp}}\int_0^{T_{sp}}I_{i,H}\left(u',w'\right)dt \tag{B.4}$$

Appendix C. Supplementary data

Supplementary material related to this article can be found online at https://doi.org/10.1016/j.agrformet.2023.109522.

References

Bates, E.M., Lombard, P.B., et al., 1978. Evaluation of Temperature Inversions and Wind Machine on Frost Protection in Southern Oregon. Oregon Agricultural Experiment Station, https://ir.library.oregonstate.edu/concern/administrative_report_or_publications/tb09j657w.

Battany, M.C., 2012. Vineyard frost protection with upward-blowing wind machines. Agricult. Forest Meteorol. 157, 39–48. http://dx.doi.org/10.1016/j.agrformet.2012.01.009.

Beyá-Marshall, V., Herrera, J., Santibáñez, F., Fichet, T., 2019. Microclimate modification under the effect of stationary and portable wind machines. Agricult. Forest Meteorol. 269, 351–363. http://dx.doi.org/10.1016/j.agrformet.2019.01.042.

Boekee, J., Dai, Y., Schilperoort, B., van de Wiel, B.J., ten Veldhuis, M.-C., 2023. Plant–atmosphere heat exchange during wind machine operation for frost protection. Agricult. Forest Meteorol. 330, 109312. http://dx.doi.org/10.1016/j.agrformet.2023.109312.

Brooks, F., Rhoades, D., Leonard, A., et al., 1952. Wind machines: 90 and 15 bhp machines compared for frost protection at riverside. Calif. Agric. 6 (8), 7–8, https://hilgardia.ucanr.edu/Abstract/?a=ca.v006n08p7.

Brooks, F., Rhoades, D., Leonard, A., et al., 1954. Wind machine tests in citrus: frost protection studies in 1954 confirmed earlier findings next to be investigated in deciduous trees. Calif. Agric. 8 (8), 8–10.

Brooks, F., Schultz, H., et al., 1958. Orchard heating effectiveness: Protection against radiation frosts by orchard heaters and by wind machines alone and in combination compared. Calif. Agric. 12 (8), 4–13, https://calag.ucanr.edu/Archive/?article=ca.v012n08p4.

Brunet, Y., 2020. Turbulent Flow in Plant Canopies: Historical Perspective and Overview, Vol. 177. Springer, pp. 323–324. http://dx.doi.org/10.1007/s10546-020-00560-7, chapter 3.

Davis, R., 1977. An evaluation of frost protection provided by a wind machine in the Okanagan valley of British Columbia. Can. J. Plant Sci. 57 (1), 71–74. http://dx.doi.org/10.4141/cjps77-011.

des Tombe, B.F., Schilperoort, B., Python distributed temperature sensing calibration. http://dx.doi.org/10.5281/zenodo.1410097. URL https://github.com/dtscalibration/python-dts-calibration.

des Tombe, B., Schilperoort, B., Bakker, M., 2020. Estimation of temperature and associated uncertainty from fiber-optic raman-spectrum distributed temperature sensing. Sensors 20 (8), 2235. http://dx.doi.org/10.3390/s20082235.

Evans, R.G., 1999. Frost Protection in Orchards and Vineyards. Washington State Univ. Coop. Ext. Pullman.

Fisher, K.H., 2009. Reducing cold injury to grapes through the use of wind machines.

Frith, H., 1951. Frost protection in orchards using air from the temperature inversion layer. Aust. J. Agric. Res. 2 (1), 24–42. http://dx.doi.org/10.1071/AR9510024.

Goodall, G., Angus, D., Leonard, A., Brooks, F., et al., 1957. Effectiveness of wind machines: Frost protection by ramjet or conventional wind machines in deciduous orchards depends on the strength of the inversion. Calif. Agric. 11 (8), 7–9, https://calag.ucanr.edu/Archive/?article=ca.v011n08p7.

Heusinkveld, V.W., van Hooft, J.A., Schilperoort, B., Baas, P., van de Wiel, B.J., et al., 2020. Towards a physics-based understanding of fruit frost protection using wind machines. Agricult. Forest Meteorol. 282, 107868. http://dx.doi.org/10.1016/j.agrformet.2019.107868.

Hu, Y., Asante, E.A., Lu, Y., Mahmood, A., Buttar, N.A., Yuan, S., 2018. Review of air disturbance technology for plant frost protection. Int. J. Agric. Biol. Eng. 11 (3), 21–28. http://dx.doi.org/10.25165/j.ijabe.20181103.3172.

Kimura, K., Yasutake, D., Nakazono, K., Kitano, M., 2017. Dynamic distribution of thermal effects of an oscillating frost protective fan in a tea field. Biosyst. Eng. 164, 98–109. http://dx.doi.org/10.1016/j.biosystemseng.2017.09.010.

Lamichhane, J.R., 2021. Rising risks of late-spring frosts in a changing climate. Nature Clim. Change 11 (7), 554–555. http://dx.doi.org/10.1038/s41558-021-01090-x.

Lee, X., Black, T.A., 1993. Atmospheric turbulence within and above a Douglas-fir stand. Part II: Eddy fluxes of sensible heat and water vapour. Bound.-Lay. Meteorol. 64 (4), 369–389. http://dx.doi.org/10.1007/BF00711706.

Liu, Q., Piao, S., Janssens, I.A., Fu, Y., Peng, S., Lian, X., Ciais, P., Myneni, R.B., Peñuelas, J., Wang, T., 2018. Extension of the growing season increases vegetation exposure to frost. Nature Commun. 9 (1), 1–8. http://dx.doi.org/10.1038/s41467-017-02690-y.

Liubchenkova, N., 2021. Euronews: 'historic' bout of frost decimates french winemakers' harvest. Accessed: 2022-05-09. https://www.euronews.com/my-europe/2021/04/10/historic-bout-of-frost-decimate-french-winemakers-harvest.

Lu, S., Willmarth, W., 1973. Measurements of the structure of the Reynolds stress in a turbulent boundary layer. J. Fluid Mech. 60 (3), 481–511. http://dx.doi.org/10.1017/S0022112073000315.

Oliver, C., 2012. Near field mixing of negatively buoyant jets. http://dx.doi.org/10.26021/3017.

Perry, K.B., 1998. Basics of frost and freeze protection for horticultural crops. HortTechnology 8 (1), 10–15. http://dx.doi.org/10.21273/HORTTECH.8.1.10.

Raupach, M., 1981. Conditional statistics of Reynolds stress in rough-wall and smooth-wall turbulent boundary layers. J. Fluid Mech. 108, 363–382. http://dx.doi.org/10.1017/S0022112081002164.

Raupach, M., Coppin, P., Legg, B., 1986. Experiments on scalar dispersion within a model plant canopy part I: The turbulence structure. Bound.-Lay. Meteorol. 35 (1), 21–52. http://dx.doi.org/10.1007/BF00117300.

Rhoades, D., Brooks, F., Leonard, A., Schultz, H., et al., 1955. Frost protection in almonds: Wind machine studies in 1955 frost season indicate protection in mature almond orchards below that obtained in citrus. Calif. Agric. 9 (8), 3–14, https://calag.ucanr.edu/Archive/?article=ca.v009n08p3.

Ribeiro, A.C., De Melo-Abreu, J.P., Snyder, R.L., 2006. Apple orchard frost protection with wind machine operation. Agricult. Forest Meteorol. 141 (2–4), 71–81. http://dx.doi.org/10.1016/j.agrformet.2006.08.019.

Schilperoort, B., Coenders-Gerrits, M., Jiménez Rodríguez, C., van der Tol, C., Van De Wiel, B., Savenije, H., 2020. Decoupling of a douglas fir canopy: a look into the subcanopy with continuous vertical temperature profiles. Biogeosciences 17 (24), 6423–6439. http://dx.doi.org/10.5194/bg-17-6423-2020.

Siegmund, P., 2022. KNMI climate report growing season has longer and longer frost. Accessed: 2022-05-09. https://www.knmi.nl/over-het-knmi/nieuws/groeiseizoen-kent-steeds-langer-nachtvorst.

Thomas, C.K., Kennedy, A.M., Selker, J.S., Moretti, A., Schroth, M.H., Smoot, A.R., Tufillaro, N.B., Zeeman, M.J., 2012. High-resolution fibre-optic temperature sensing: A new tool to study the two-dimensional structure of atmospheric surface-layer flow. Bound.-Lay. Meteorol. 142 (2), 177–192. http://dx.doi.org/10.1007/s10546-011-9672-7.

Yue, W., Meneveau, C., Parlange, M.B., Zhu, W., Van Hout, R., Katz, J., 2007. A comparative quadrant analysis of turbulence in a plant canopy. Water Resour. Res. 43 (5), http://dx.doi.org/10.1029/2006WR005583.